Platinum hydride formation during cathodic corrosion in aqueous solutions

Hersbach, T.J.P.; Garcia-Esparza, A.T.; Hanselman, S.R.; Paredes Mellone, O.A.; Hoogenboom, T.; Mccrum, I.T.; ... ; Sokaras, D., Koper, M.T.M.

Citation

Hersbach, T. J. P., Garcia-Esparza, A. T., Hanselman, S. R., Paredes Mellone, O. A., Hoogenboom, T., Mccrum, I. T., ... Sokaras, D. , K. , M. T. M. (2025). Platinum hydride formation during cathodic corrosion in aqueous solutions. *Nature Materials*, *24*(4), 574–580. doi:10.1038/s41563-024-02080-y nature materials

Article

https://doi.org/10.1038/s41563-024-02080-y

Platinum hydride formation during cathodic corrosion in aqueous solutions

Received: 17 May 2023

Accepted: 12 November 2024

Thomas J. P. Hersbach [1,2], Angel T. Garcia-Esparza [2], Selwyn Hanselman [1], Oscar A. Paredes Mellone [2], Thijs Hoogenboom [1,3], Ian T. McCrum [4], Dimitra Anastasiadou [1], Jeremy T. Feaster [5,6,9], Thomas F. Jaramillo [5,6], John Vinson [7], Thomas Kroll [2], Amanda C. Garcia [1,10], Petr Krtil [8], Dimosthenis Sokaras [2] & Marc T. M. Koper [1]

Cathodic corrosion is an electrochemical phenomenon that etches metals at moderately negative potentials. Although cathodic corrosion probably occurs by forming a metal-containing anion, such intermediate species have not yet been observed. Here, aiming to resolve this long-standing debate, our work provides such evidence through X-ray absorption spectroscopy. High-energy-resolution X-ray absorption near-edge structure experiments are used to characterize platinum nanoparticles during cathodic corrosion in 10 mol l^{-1} NaOH. These experiments detect minute chemical changes in the Pt during corrosion that match first-principles simulations of X-ray absorption spectra of surface platinum multilayer hydrides. Thus, this work supports the existence of hydride-like platinum during cathodic corrosion. Notably, these results provide a direct observation of these species under conditions where they are highly unstable and where prominent hydrogen bubble formation interferes with most spectroscopy methods. Therefore, this work identifies the elusive intermediate that underlies cathodic corrosion.

Electrocatalysis will play an increasing role this century, as renewable resources replace fossil-based energy and chemicals. In electrocatalysis-driven industries, metallic electrodes will routinely reach strongly negative potentials while catalysing hydrogen formation, ammonia production, carbon dioxide and monoxide reduction or biomass hydrogenation. Although most metals are assumed to be stable in their elemental state under these conditions[1], this supposition can be challenging to verify. This consideration is particularly pressing for platinum, which is commonly used as a stable electrode and for which the anodic limitations have long been known[2], but for which cathodic transformations are much less explored. The cathodic stability of metals should therefore not be taken for granted, as counter-intuitive chemical changes can occur at negative potentials.

Cathodic corrosion is such a process that etches many metals[3,4]. Despite extensive research on cathodic corrosion[5–7], its chemical origins are still not understood. This knowledge gap stems from two factors. First, vigorous hydrogen evolution during corrosion impairs in situ studies. Second, the main corrosion intermediates are short-lived

---

[1]Leiden Institute of Chemistry, Leiden University, Leiden, The Netherlands. [2]Stanford Synchrotron Radiation Lightsource, SLAC National Accelerator Laboratory, Menlo Park, CA, USA. [3]Leiden Institute of Physics, Leiden University, Leiden, The Netherlands. [4]Department of Chemical and Biomolecular Engineering, Clarkson University, Potsdam, NY, USA. [5]SUNCAT Center for Interface Science and Catalysis, SLAC National Accelerator Laboratory, Menlo Park, CA, USA. [6]Department of Chemical Engineering, Stanford University, Stanford, CA, USA. [7]Material Measurement Laboratory, National Institute of Standards and Technology, Gaithersburg, MD, USA. [8]J. Heyrovský Institute of Physical Chemistry of the Czech Academy of Sciences, Prague, Czech Republic. [9]Present address: Materials Science Division, Lawrence Livermore National Laboratory, Livermore, CA, USA. [10]Present address: Faculty of Science, Van 't Hoff Institute for Molecular Sciences, University of Amsterdam, Amsterdam, The Netherlands. e-mail: dsokaras@slac.stanford.edu; m.koper@lic.leidenuniv.nl

and cannot be isolated for ex situ characterization; instead, only corroded metallic surfaces[8] or the metal (oxide) nanoparticle products of cathodic corrosion have been studied[4,9,10]. Through these indirect observations, cathodic corrosion is hypothesized to occur via metal anions[11] or ternary metal hydrides[8]. Neither species has yet been observed during cathodic corrosion, so it is imperative to use operando techniques to probe corrosion intermediates.

Operando characterization typically relies on spectroscopy to probe a sample's oxidation state or chemical environment. However, most spectroscopies are incompatible with the challenging working conditions during cathodic corrosion[12]. A suitable technique for studying cathodic corrosion is X-ray absorption near-edge structure (XANES) spectroscopy, which can probe Pt *d*-band filling, Pt oxidation state and the presence of adsorbates[13–16]. We use operando XANES to study Pt during cathodic corrosion, using a custom-made flow cell to minimize interference from electrogenerated hydrogen bubbles. Furthermore, we utilize the high-energy resolution fluorescence detection (HERFD) configuration, which sharpens the Pt L_{III} XANES spectrum and greatly enhances detection sensitivity. Our experiments reveal spectral changes that, compared with theoretically modelled XANES spectra, support the existence of hydride-like platinum during cathodic corrosion. This work detects these species under aqueous conditions, which is particularly notable when considering that such hydrides are extremely moisture-sensitive and often synthesized at high temperatures and pressures[17,18]. Thus, our results indicate that metal electrodes can form unexpected species under electrocatalytically relevant conditions.

Results and discussion

Before presenting our results, we will outline the species that might underlie cathodic corrosion. The first of these is a metallide: a monometallic anion such as a platinide (Pt^{n-})[11]. Whereas metallides are moisture-sensitive, bulk platinides have been synthesized[19,20] and dissolved argentides and aurides can form in ammonia[21,22]. Another candidate is a ternary metal hydride, composed of hydrogen, a noble metal and an alkali or alkaline earth cation[8,23]. Many such hydrides have been synthesized, including Na_2PtH_4 and Na_2PtH_6 (refs. 17,18). Between these candidates, recent literature has favoured ternary metal hydrides[8,24–26].

Two important observations support ternary metal hydrides over metallides. First, among metallides, forming aurides is more energetically favourable than forming rhodides or platinides[27]. This trend contrasts with cathodic corrosion onset potentials, which are approximately 0.3 V less negative for platinum and rhodium than for gold[8,28,29]. Second, forming metal hydrides requires a hydrogen source such as water, whereas metallide formation does not. Notably, cathodic corrosion does not proceed without water present[24]. Thus, previous results favour the ternary metal hydride hypothesis. However, drawing definitive mechanistic conclusions requires operando experiments.

Therefore, we present operando XANES at the Pt L_{III} absorption edge during cathodic corrosion in 10 mol l^{-1} NaOH. Such experiments can distinguish metallides and hydrides because each species should produce distinct X-ray absorption fingerprints. To our knowledge, so far, no XANES spectra for platinum metallides and hydrides have been reported. Related auride spectra have been published[30] but offer limited insight for predicting platinum behaviour. Given this lack of benchmarks, platinum metallide and hydride XANES spectra need to be calculated.

Modelled XANES spectra

Our XANES spectra simulations rely on the first-principles OCEAN package[31], for which we used theoretical Na_2Pt, NaPt and Na_2Pt (ref. 32), experimental Na_2PtH_4 and Na_2PtH_6 (refs. 17,33) and theoretical platinum surface supercell slabs with one to four monolayers (MLs) of hydrogen as input structures[25]. The latter structures were simulated as intermediates for platinum hydride formation, and their likely existence is both theoretically and experimentally supported. For example, Pt reaches hydrogen coverages of up to two MLs around −0.3 V versus the reversible hydrogen electrode (V_{RHE}) in acid[34,35]. At lower voltages where corrosion occurs, computational efforts have suggested hydrogen coverages as high as 1.6–2.4 times the coverage at 0 V_{RHE} (refs. 36,37). Notably, these studies did not consider platinum surface reconstructions, which hydrogen can induce at coverages slightly above one ML[38]. Other work did allow surface reconstruction but did not include multilayer hydrogen coverages[26]. Thus, we recently probed the effects of high hydrogen coverages and surface reconstruction simultaneously[25], showing adsorption of up to four MLs of hydrogen to be energetically possible and restructure the hydrogen-covered platinum surfaces. We use the resulting structures here to generate OCEAN-based XANES spectra.

For Pt surfaces with *H multilayers, our analysis omits crystal facet dependencies and the presence of *Na that probably co-adsorbs during cathodic corrosion[8]. These omissions were made to reduce the complexity and cost of our computations at higher *H coverages[25] after verifying that surface structure and cation adsorption had negligible effects on OCEAN spectra of hydrogen MLs (Supplementary Figs. 9 and 10). Supplementary spectra were also calculated for bulk α-PtO_2 to benchmark the computational protocol to our experimental results (Supplementary Figs. 8 and 16).

For the hydrogen-covered platinum surfaces and bulk platinides, OCEAN-simulated spectra and difference spectra are shown in Fig. 1. This Figure displays normalized absorption (μ_n) on the y-axis, in units of 'edge fraction'. Here, when comparing the spectra of Pt without *H and with one-ML *H (Fig. 1a), hydrogen adsorption decreases the whiteline peak intensity and creates a shoulder extending to 11,578 eV. These differences are emphasized in the difference spectrum that results from subtracting the bare Pt spectrum from that with one-ML *H (Fig. 1). By subtracting this spectrum, we remove contributions from electrochemically inactive bulk Pt atoms, and emphasize spectral differences that are caused by changes of the surface atoms[39]. For the difference spectra in Fig. 1c, the 'fingerprint' of one-ML *H contains a negative feature at 11,564.6 eV, crosses $\Delta\mu_n = 0$ at 11,566.0 eV and features a shoulder that peaks at 11,567.0 eV before gradually decreasing. The theoretical spectra for higher hydrogen coverages in Fig. 1 have similar features: a lower peak intensity than at a coverage of one ML and a shoulder at energies above 11,567.0 eV. Importantly, the difference spectra at two- to four-ML *H coverage resemble that of one-ML *H, except their magnitude is 1.9–2.3 times higher and they cross $\Delta\mu_n = 0$ at slightly higher energies (11,566.2–11,566.4 eV). Analogously, bulk Na_2PtH_4 and Na_2PtH_6 hydrides have similar difference spectra with higher intensities (Supplementary Fig. 8) compared with those in Fig. 1. Although the height of the whiteline peak in Fig. 1a decreases at increasing *H coverage, the overall peak area remains similar because the peak broadens: the whiteline integral increases by 2% to 25% for the multilayers when integrating up to 11,580 eV with a linear baseline at $\mu_n = 1$ edge fraction.

Importantly, the data in Fig. 1 for one hydrogen ML match with XANES spectra for hydrogen-covered Pt in literature[15,16] and our experimental difference spectra of Pt at 0 V_{RHE} (Supplementary Fig. 16). This agreement indicates that OCEAN captures the behaviour of Pt and that forming a platinum hydride produces spectral shifts to higher X-ray energies, crosses $\Delta\mu_n = 0$ between 11,566.2 and 11,566.4 eV, yields a high-energy shoulder in difference spectra and increases the difference spectrum magnitude at increasing hydrogen coverages.

The analysis for hydrogen-covered platinum is replicated for platinides in Fig. 1b,d. Here, the spectra of $NaPt_2$, NaPt and Na_2Pt are broader and less intense than metallic Pt. This suppressed intensity matches auride XANES spectra[30] and indicates platinum *d*-band filling. Each platinide absorbs more strongly than metallic platinum above 11,568 eV and exhibits distinct difference spectra: $NaPt_2$ peaks negatively at 11,565.0 eV and has a broad positive shoulder that peaks around 11,572.3 eV; NaPt has a negative peak at 11,565.3 eV with slowly

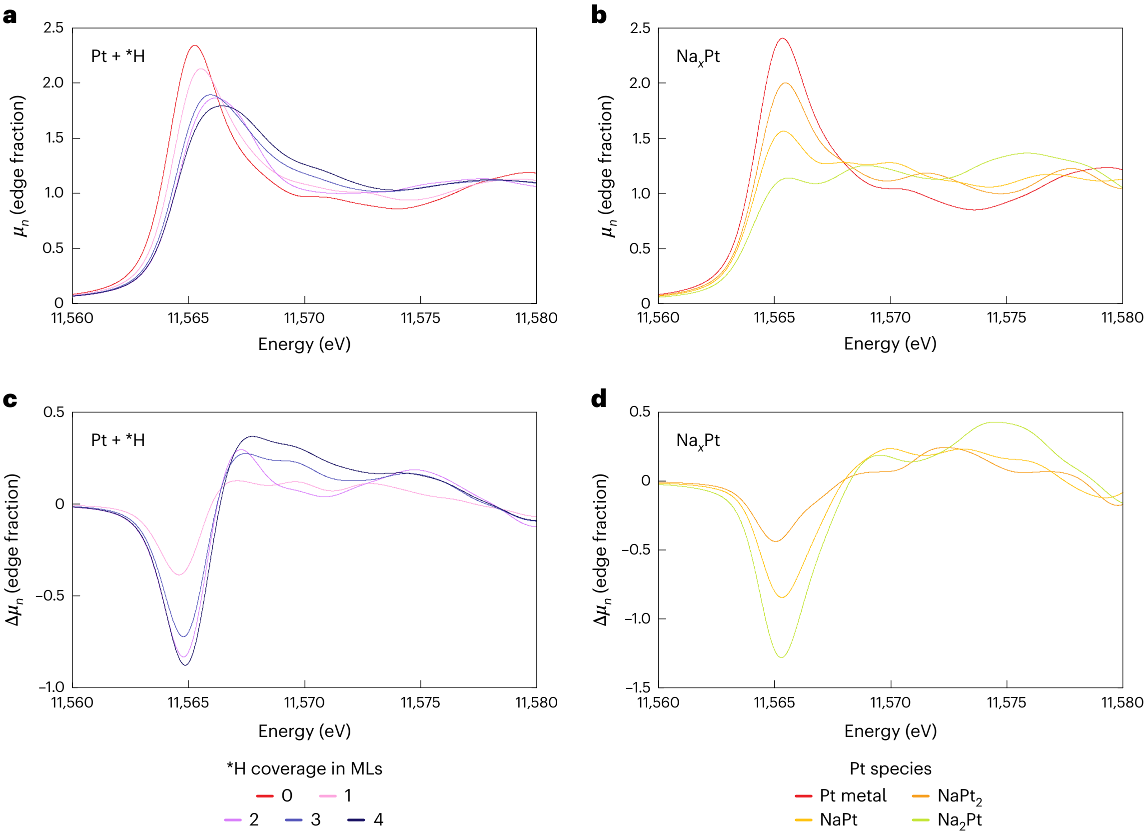

Fig. 1 | OCEAN-based spectra for hydrogen-covered platinum and bulk platinides. a,c, Theoretical first-principles calculations of Pt L_{III} edge X-ray absorption spectra of platinum with zero through four MLs of *H on Pt(111) (**a**), and corresponding difference spectra that are obtained by subtracting the spectrum of bare Pt(111) from those with one through four MLs of *H (**c**). **b**,**d**, Analogous spectra are shown for bulk metallic platinum and platinides (**b**), for which difference spectra are obtained by subtracting the bulk Pt metal spectrum from the bulk platinide spectra (**d**).

rising intensity peaking at 11,570.0 eV; and Na_2Pt peaks sharply negative at 11,565.3 eV with two positive peaks at 11,569.4 and 11,574.5 eV. Each platinide crosses $\Delta\mu_n = 0$ at progressively higher energies, between 11,567.9 eV ($NaPt_2$) and 11,568.3 eV (Na_2Pt). The whiteline integral decreases slightly, up to 18% for Na_2Pt when integrating up to 11,580 eV with a linear baseline at $\mu_n = 1$ edge fraction. Overall, Fig. 1b,d suggests that platinide formation would produce spectral broadening and intensity shifts to higher energies. Notably, the difference spectra in Fig. 1d differ from those for hydrogen-covered platinum in Fig. 1c: platinide difference spectra rise gradually in intensity after their initial negative feature, crossing $\Delta\mu_n = 0$ at approximately 11,568 eV, while producing a slowly increasing shoulder at higher X-ray energies. These features differ from those expected for platinum hydrides: hydride difference spectra rise more sharply and at lower energies than their platinide counterparts, crossing $\Delta\mu_n = 0$ at 1.5–1.9 eV lower energies and dropping off in intensity relatively monotonically as X-ray energies increase. Thus, high-energy-resolution fluorescence detection (HERFD)-XANES difference spectra should be able to distinguish platinides and platinum hydrides. With these predictions, the experimental behaviour of platinum during cathodic corrosion can be evaluated.

Absorption spectra at cathodic potentials

Experimental HERFD-XANES spectra for platinum nanoparticles are shown in Fig. 2. Spectra at negative potentials are shown in Fig. 2a to study cathodic corrosion. Corresponding difference spectra (Fig. 2b) are obtained by subtracting the spectrum at 0.4 V_{RHE} from the other spectra. Smoothed spectra were used in Fig. 2b to help visualize the data[39]; unsmoothed difference spectra are shown in Supplementary Figs. 13 and 14. We also validated our experiments by recording spectra at oxidative voltages. This test, shown in Supplementary Fig. 15, reproduces previously reported spectra at anodic voltages[16], thus confirming that we can detect electrochemical changes of the working electrode.

After validating our experimental sensitivity, we probe spectral changes at cathodic potentials (Fig. 2a). In Fig. 2a, the spectrum at the highest electrode potential was recorded at 0 V_{RHE}. This spectrum resembles the spectrum at 0.4 V_{RHE} (Supplementary Fig. 17) but has a reduced whiteline peak intensity and is somewhat broader due to adsorbed hydrogen that covers 60–100% of the platinum surface at 0 V_{RHE} (refs. 14,16,35,40). Indeed, the difference spectrum at 0 V_{RHE} (Fig. 2b) matches previous experiments[16] and theoretical difference spectra of ML-covered platinum (Supplementary Fig. 16).

The whiteline broadening persists at lower potentials (Fig. 2a) and is paired with an absorption edge shift towards positive energies as the applied potential is lowered: the shift between 0 V_{RHE} and −1.0 V_{RHE} is 0.1 eV. This shift and corresponding spectral broadening are subtle but systematic, as shown by the appearance of a high-energy peak in Supplementary Figs. 18 and 19 and Supplementary Table 1. These changes are visualized in the cathodic difference spectra (Fig. 2b): below 0 V_{RHE}, the difference spectrum contains a sharp negative peak at 11,564.4 eV and a broad positive shoulder above 11,566 eV. Although this difference spectrum shape remains similar as the electrode potential is lowered, the difference spectrum magnitude increases when stepping from 0 V_{RHE} to −0.4 V_{RHE} and −0.6 V_{RHE}, and increases again at −0.8 V_{RHE} and −1.0 V_{RHE}. Overall, Fig. 2 indicates that cathodic corrosion broadens the Pt whiteline without reducing its peak area (Supplementary Fig. 19); these changes yield difference spectra with a broad shoulder and an increasing magnitude at increasingly negative potentials. The difference spectra cross $\Delta\mu_n = 0$ at 11,566.5 eV and 11,566.0 eV at −0.8 V_{RHE}

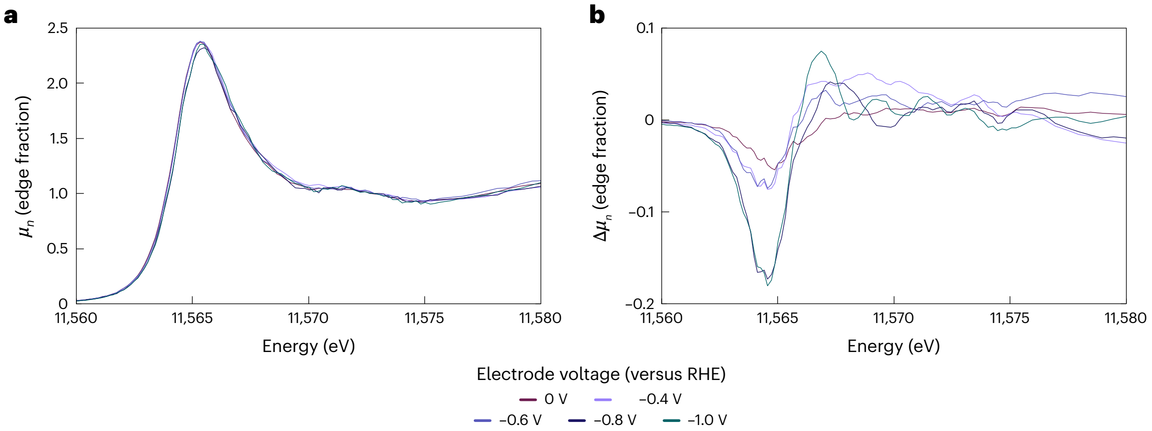

Fig. 2 | Experimental HERFD-XANES spectra for platinum nanoparticles. **a**,**b**, Pt L_{III}-edge HERFD-XANES spectra (**a**) and smoothed difference spectra (**b**) of electrodes polarized at cathodic potentials in 10 mol l^{-1} NaOH. Potentials are presented against the RHE scale. The spectra in **a** are unsmoothed, whereas the difference spectra in **b** were obtained from smoothed spectra as follows. Difference spectra were calculated by smoothing the spectra in **a** and then subtracting the smoothed spectrum of Pt at 0.4 V_{RHE} from the other smoothed spectra. Unsmoothed difference spectra are shown in Supplementary Information, which contains further details on the smoothing procedure.

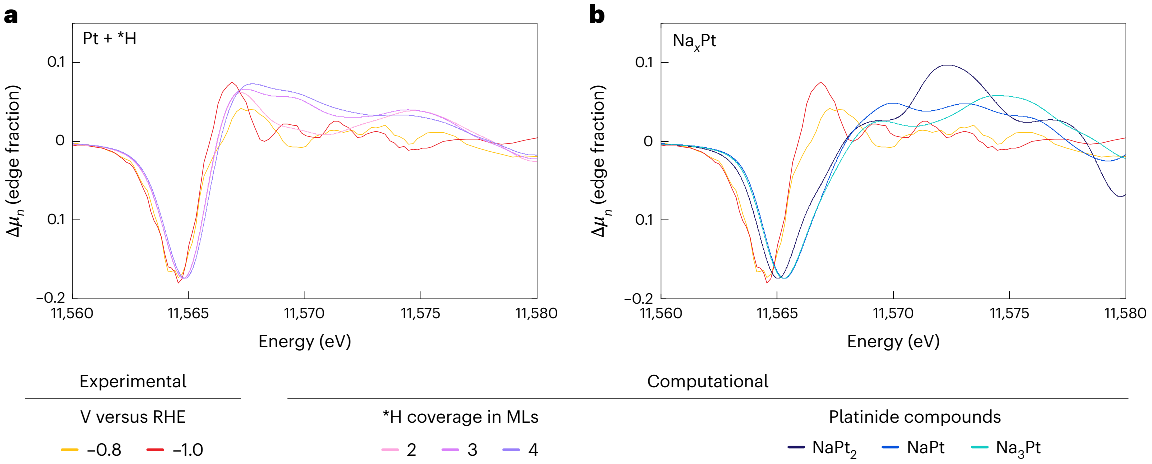

Fig. 3 | Comparison of experimental and computational HERFD-XANES difference spectra. **a**,**b**, Experimental difference spectrum of electrodes polarized at −0.8 V_{RHE} and −1.0 V_{RHE}, plotted alongside the rescaled theoretical difference spectra for Pt(111) with two, three and four MLs of *H (**a**) and plotted against the rescaled theoretical difference spectra of platinides (**b**). For the data, the reference spectrum was that at 0.4 V_{RHE}. The difference spectra match their respective versions in Figs. 1 and 2, except that the theoretical difference spectra were rescaled to match the magnitude of the experimental difference spectrum.

and −1.0 V_{RHE}, respectively. These changes align closely with the formation of platinum hydrides while matching poorly with the features that accompany platinide formation. Thus, Fig. 2 indicates platinum hydride formation during cathodic corrosion.

This match is explored in Fig. 3, which compares the experimental difference spectrum at −0.8 V_{RHE} and −1.0 V_{RHE} with the theoretical difference spectra for hydrogen-covered platinum and platinum hydrides. In Fig. 3, the calculated difference spectra are rescaled to match the magnitude of their experimental counterparts. Such rescaling helps compare the characteristic shape that indicates the type of surface adsorbate, whereas the magnitude is indicative of adsorbate coverages and the surface-to-bulk ratio of the studied Pt material[39]. As Fig. 3a shows, the experimental and theoretical difference spectra match well for platinum with *H multilayers: they have a sharp minimum around 11,565 eV, followed by a positive feature that slowly decreases in height towards 11,580 eV, and crossing $\Delta\mu_n = 0$ at similar energies. By contrast, the match is poor for platinides (Fig. 3b): our experimental difference spectrum rises more sharply after its negative feature while missing the positive signal above 11,572 eV that would evidence platinide formation. In other words, Fig. 3 suggests the formation of hydrogen multilayers during cathodic corrosion.

This theory–experiment match is encouraging but could also be explained by the creation of platinum surface area during cathodic corrosion. After all, the expected difference spectra for Pt with one hydrogen ML predominantly differ from those for two to four MLs in terms of magnitude, whereas the difference spectrum shapes are similar for all coverages (Fig. 1). This similarity means that the increasing experimental difference spectrum magnitude in Fig. 2b could be explained by a surface area increase during cathodic corrosion, which would expose platinum to be covered by a hydrogen ML. This hypothesis is explored in Supplementary Fig. 20, which reveals no signs of a surface area increase.

Another hypothesis invokes adsorbed *OH below 0 V_{RHE}, which was suggested to exist through X-ray photoelectron spectroscopy (XPS) in 2018[41]. If present, this *OH might desorb between 0 V_{RHE} and −1.0 V_{RHE}, causing changes resembling those in Fig. 2b. However, density functional theory (DFT) and voltammetry have shown that *OH does not co-adsorb with *H at these potentials[42]. Indeed, recent vibrational spectroscopy experiments showed that no *OH adsorbs on Pt below 0.25 V_{RHE} (ref. 43). Therefore, *OH desorption cannot explain any changes in Fig. 2b below 0 V_{RHE}.

In short, cathodic corrosion broadens the platinum L_{III} whiteline and yields a positive absorption edge shift. This change is systematic,

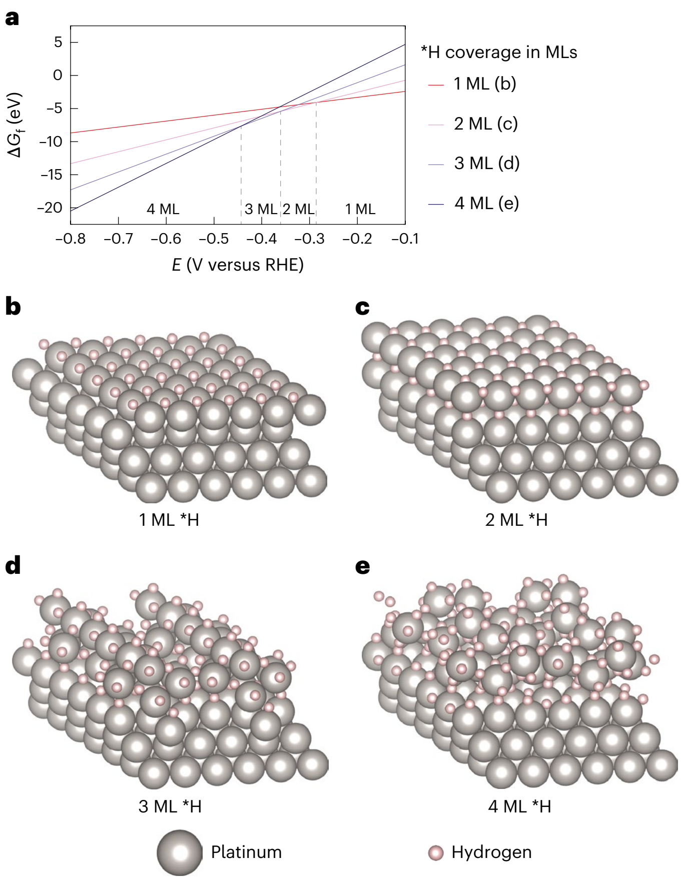

Fig. 4 | Phase diagram and surface models of hydrogen-covered platinum. a, A computed phase diagram plotting the thermodynamically most favourable hydrogen coverage on Pt(111) as a function of electrode potential. **b**–**e**, Space-filling representations of the thermodynamically most favourable structures underlying the phase diagram (1 ML (**b**), 2 ML (**c**), 3 ML (**d**) and 4 ML (**e**)). The one-ML *H visualization in **b** corresponds to so-called underpotential deposited (UPD) hydrogen. Each panel contains 2 × 2 unit cells and was rendered using VESTA[47].

does not markedly decrease the whiteline area (Supplementary Fig. 19) and yields characteristic difference spectra at −0.8 V_{RHE} and −1.0 V_{RHE}. We compared these observations to theoretical spectra, for which Pt with two- to four-ML *H closely resembles the experimental difference spectra during corrosion (Fig. 3). Importantly, the results in Figs. 2b and 3 cannot be explained by the presence of sodium platinides, the creation of platinum surface area or *OH desorption. Thus, the theory–experiment match in Fig. 3 strongly suggests that platinum is covered with hydrogen multilayers during cathodic corrosion.

Importantly, these structures were obtained from our DFT work that explored whether multilayer hydrogen coverages are thermodynamically feasible[25]. Key results from this work are reproduced in Fig. 4, which offers insights into the present work. Figure 4a shows a phase diagram, displaying the most thermodynamically stable hydrogen coverage as function of the applied voltage. The diagram shows that Pt is covered with one ML of hydrogen above −0.29 V_{RHE}. Below this potential, two MLs are favourable, followed by three MLs at −0.36 V_{RHE} and four MLs at −0.44 V_{RHE}. These potentials match the −0.4 V_{RHE} onset of cathodic platinum corrosion in 10 mol l^{-1} NaOH (ref. 28).

Models of these surfaces are shown in Fig. 4b–e. Figure 4b shows adsorbed hydrogen in the typical threefold *fcc* hollow position for a coverage of one ML[40]. Strikingly, the most stable structure for two MLs contains subsurface hydrogen (Fig. 4c), which contrasts with experimental observations of the second hydrogen ML adsorbing atop Pt atoms[34]. We attribute this discrepancy to the current work not accounting for kinetic barriers that might disfavour the structure in Fig. 4c. At higher coverages of three and four MLs (Fig. 4d,e), adsorbed hydrogen rearranges the top platinum layer. Notably, as visualized in Supplementary Fig. 11 (which shows platinum–hydrogen bonds with distances below 1.9 Å), adsorbing three-ML *H creates highly hydrogen-coordinated platinum: between the nine top-layer Pt atoms in each 3 × 3 unit cell, one is threefold hydrogen-coordinated, five are fourfold coordinated and three are fivefold coordinated. If one also includes 1.95 Å and 1.97 Å Pt–H distances as bonds, the top nine atoms contain three fourfold, two fivefold and four sixfold hydrogen-coordinated Pt atoms. This highly coordinated Pt persists at four-ML *H coverage, where the top layer contains two fourfold, five fivefold and two sixfold hydrogen-coordinated Pt atoms (Pt–H distance <1.9 Å). When also counting Pt–H bonds up to 2.0 Å, there are one fourfold-, three fivefold- and five sixfold-coordinated Pt atoms. In other words, Fig. 4 indicates that adsorbing three or four *H MLs creates highly hydrogen-coordinated platinum. More specifically, the Pt–H configurations resemble the square planar and octahedral hydrogen coordination of platinum in bulk Na_2PtH_4 and Na_2PtH_6 (Supplementary Figs. 7 and 11). These geometries are stable at the onset potentials of platinum corrosion (Fig. 4a)[8]. Thus, our previous theoretical work (Fig. 4) indicates that hydride-like platinum can form under cathodic corrosion conditions[25], whereas the present XANES results (Figs. 1–3) reveal the spectral signatures of these hydrides.

These multilayer-covered surfaces have similar spectral magnitudes (Fig. 1), which precludes the exact determination of *H coverages during corrosion. However, the difference spectrum magnitude during corrosion does allow estimations of the amount of surface atoms that participate in cathodic corrosion. After all, Fig. 1c suggests that, if all surface atoms partake in cathodic corrosion, the difference spectrum magnitude should increase by 1.9–2.3 times. This change is slightly lower than the approximate threefold magnitude increase when going from 0 V_{RHE} to −0.8 V_{RHE} (Fig. 2), thus indicating that all Pt surface atoms bind to hydrogen in a manner reflecting Fig. 4b–e and that additional platinum may bind to hydrogen as corrosion induces reconstruction.

Although our work cannot probe exact hydrogen coverages during cathodic corrosion, our computations suggest that coverages increase as the electrode potential is lowered[25]. Fundamentally, these calculations indicate that disordering platinum surfaces is energetically favourable at hydrogen coverages of ≥3 monolayers (Fig. 4), which might play a role in reorganizing Pt surfaces during cathodic corrosion. In other words, hydrogen adsorption might, together with cation adsorption[8], drive cathodic corrosion: the exact corrosion onset potential and anisotropic etching characteristics would result from an interplay between cations and hydrogen[8,25].

We further illustrate this point by focusing on the Pt–H coordination environment. At high hydrogen coverages, Pt atoms are four- to sixfold coordinated to hydrogen (Supplementary Fig. 11) and transfer a fraction of their charge (≤0.12 e^-) to the hydrogen[25], thus resembling platinum in Na_2PtH_4 and Na_2PtH_6 (Supplementary Fig. 7)[18]. Dissolving these structures after initial disorganization of the surface would require cations[12], much like forming CO_2^- intermediates during CO_2 reduction does[44].

Our conclusions align with XPS results that suggest hydride formation around −0.2 V_{RHE} in 1 mol l^{-1} KOH[41], approximately 0.3–0.4 V before the onset of cathodic corrosion under those conditions[8], where hydrogen multilayers are not expected (Fig. 4). Likewise, our work is supported by infrared (IR) spectroscopy observing overpotential deposited hydrogen, which reaches near-full coverages between −0.1 V_{RHE} and −0.3 V_{RHE} in acidic conditions[34,35]. The present work expands on these results in two key manners: it operates during the challenging working conditions of cathodic corrosion (−1.0 V_{RHE}) while adding the superior chemical sensitivity of HERFD-XANES that can separate Pt hydrides from platinides.

In terms of working conditions, the aforementioned XPS and IR studies did not reach the cathodic corrosion onset voltage, probably due to their incompatibility with the intense hydrogen evolution currents and bubble formation occurring during cathodic corrosion[45]. Thus, these studies illustrate what happens before cathodic corrosion but cannot elucidate what happens during corrosion. By contrast, we utilized a setup that enables spectroscopy at cathodic corrosion voltages and in 10 mol l^{-1} NaOH while maintaining the stringent cleanliness standards that are required to reliably study cathodic corrosion[8].

These operando capabilities are paired with the unique chemical specificity that HERFD-XANES and OCEAN provide. For example, unlike XPS, our methodologies are not constrained to mapping Pt oxidation states. In addition, unlike IR spectroscopy, we are not limited to detecting vibrations that match specific spectroscopic selection criteria. Instead, the current work probes the coordination environment of cathodically corroding Pt and compares experimental spectra to the first-principles-calculated spectral fingerprints of species that are unavailable as reference compounds.

Combining high-resolution chemical specificity with operando capabilities, we can both detect platinum hydrides and rule out competing cathodic corrosion hypotheses. As such, our results represent direct experimental evidence for the chemical nature of cathodic platinum corrosion. This advance is particularly relevant in light of the challenges posed by hydrogen evolution during cathodic corrosion, as well as the substantial efforts towards understanding cathodic corrosion since its discovery around 1900 and rediscovery in 2011[3,4].

Our conclusions are also relevant for the use of platinum as an inert (counter) electrode. The presumed inertness of these electrodes at voltages above 0 V_{RHE} is already known to not be guaranteed[2], but our work illustrates that platinum's stability below 0 V_{RHE} is not guaranteed either. Because such instability can be caused by ternary platinum hydrides, our contribution may spur the development of stable cathodes that are less susceptible to hydride formation.

Importantly, our conclusions extend beyond platinum. After all, we previously demonstrated that platinum, rhodium and gold respond to the presence of alkali metal ions that stabilize metal hydrides[8]. We also calculated that the corrosion of these metals can be facilitated by hydrogen adsorption[8], a conclusion that was later experimentally supported for gold[24]. Thus, our results should translate to rhodium, gold and possibly other platinum-group metals. Such translation can be aided by theoretical efforts, because the knowledge of hydride formation facilitates the calculation of DFT-based Pourbaix diagrams. These calculations will require the explicit consideration of water and cations, but they provide promising research avenues.

Finally, the demonstrated formation of ternary metal hydrides can accelerate the use of cathodic corrosion to synthesize metallic nanoparticles[46], opening up strategies towards altering nanoparticle properties by rationally tuning synthesis conditions. For example, synthesis routes could explore mixtures of water and (non-)protic solvents with differing polarities to influence hydride formation during nanoparticle synthesis[24].

Our observation of ternary platinum hydrides represents a marked advance in the understanding of cathodic corrosion, which provides the starting point for further investigations. In addition, these findings can accelerate the development of stable cathodes and guide nanoparticle synthesis. Therefore, this work is a substantial fundamental advancement that facilitates both the mitigation and utilization of cathodic corrosion.

In summary, the mechanism of cathodic corrosion has long been unknown and has been suggested to proceed via both metallide and metal hydride intermediates. Addressing this debate, we performed an operando HERFD-XANES investigation of Pt nanoparticles during cathodic corrosion. We found that cathodic corrosion shifts the Pt L_{III} absorption edge positively and broadens the whiteline peak as electrode potentials decrease. These changes match those of platinum hydride spectra that were simulated using state-of-the-art first-principles calculations. Our findings suggest that Pt is covered by hydrogen multilayers during cathodic corrosion, that charge is transferred from platinum to hydrogen and that the platinum–hydrogen coordination environment matches that of bulk metal hydrides. These observations suggest that cathodic corrosion initiates when multilayer hydrogen adsorption disorders the Pt lattice, followed by the dissolution of cation-stabilized platinum hydrides.

Ultimately, this Article provides direct indications of platinum hydrides during cathodic corrosion. This observation is particularly notable when considering the extreme water sensitivity of platinum hydrides. In addition, the high temperatures and pressures for bulk Na_2PtH_4 and Na_2PtH_6 synthesis starkly contrast the mild cathodic corrosion onset potential of −0.4 V_{RHE} at room temperature and atmospheric pressure[8,17,18,28]. Beyond cathodic corrosion, our results therefore suggest that unexpected metal-containing species might form under relatively mild electrochemical conditions. This suggestion has profound implications for our fundamental understanding of the cathodic behaviour of metals as well as for cathodic electrocatalytic experiments.

Online content

Any methods, additional references, Nature Portfolio reporting summaries, source data, extended data, supplementary information, acknowledgements, peer review information; details of author contributions and competing interests; and statements of data and code availability are available at https://doi.org/10.1038/s41563-024-02080-y.

References

1. Pourbaix, M. *Atlas of Electrochemical Equilibria in Aqueous Solutions* (National Association of Corrosion Engineers, 1974).
2. Jerkiewicz, G. Applicability of platinum as a counter-electrode material in electrocatalysis research. *ACS Catal.* **12**, 2661–2670 (2022).
3. Haber, F. The phenomenon of the formation of metallic dust from cathodes. *Trans. Am. Electrochem. Soc.* **2**, 189–196 (1902).
4. Yanson, A. I. et al. Cathodic corrosion: a quick, clean, and versatile method for the synthesis of metallic nanoparticles. *Angew. Chem. Int. Ed.* **50**, 6346–6350 (2011).
5. Arulmozhi, N., Hersbach, T. J. P. & Koper, M. T. M. Nanoscale morphological evolution of monocrystalline Pt surfaces during cathodic corrosion. *Proc. Natl Acad. Sci. USA* **117**, 32267–32277 (2020).
6. Elnagar, M. M., Hermann, J. M., Jacob, T. & Kibler, L. A. An affordable option to Au single crystals through cathodic corrosion of a wire: fabrication, electrochemical behavior, and applications in electrocatalysis and spectroscopy. *Electrochim. Acta* **372**, 137867 (2021).
7. Yang, Y. et al. Elucidating cathodic corrosion mechanisms with operando electrochemical transmission electron microscopy. *J. Am. Chem. Soc.* **144**, 15698–15708 (2022).
8. Hersbach, T. J. P. et al. Alkali metal cation effects in structuring Pt, Rh, and Au surfaces through cathodic corrosion. *ACS Appl. Mater. Interfaces* **10**, 39363–39379 (2018).
9. Bennett, E. et al. A synthetic route for the effective preparation of metal alloy nanoparticles and their use as active electrocatalysts. *ACS Catal.* **6**, 1533–1539 (2016).
10. Lawrence, M. J., Kolodziej, A. & Rodriguez, P. Controllable synthesis of nanostructured metal oxide and oxyhydroxide materials via electrochemical methods. *Curr. Opin. Electrochem.* **10**, 7–15 (2018).
11. Yanson, Y. I. & Yanson, A. I. Cathodic corrosion. I. Mechanism of corrosion via formation of metal anions in aqueous medium. *Low. Temp. Phys.* **39**, 304–311 (2013).
12. Hersbach, T. J. P. & Koper, M. T. M. Cathodic corrosion: 21st century insights into a 19th century phenomenon. *Curr. Opin. Electrochem.* **26**, 100653 (2021).

13. Friebel, D. et al. Balance of nanostructure and bimetallic interactions in Pt model fuel cell catalysts: in situ XAS and DFT study. *J. Am. Chem. Soc.* **134**, 9664–9671 (2012).
14. Merte, L. R. et al. Electrochemical oxidation of size-selected Pt nanoparticles studied using in situ high-energy-resolution X-ray absorption spectroscopy. *ACS Catal.* **2**, 2371–2376 (2012).
15. Teliska, M., O'Grady, W. E. & Ramaker, D. E. Determination of H adsorption sites on Pt/C electrodes in $HClO_4$ from Pt L_{23} X-ray absorption spectroscopy. *J. Phys. Chem. B* **108**, 2333–2344 (2004).
16. Hersbach, T. J. P. et al. Base-accelerated degradation of nanosized platinum electrocatalysts. *ACS Catal.* **11**, 9904–9915 (2021).
17. Bronger, W., Müller, P., Schmitz, D. & Spittank, H. Synthese und Struktur von Na_2PtH_4, einem ternären Hydrid mit quadratisch planaren PtH_4^{2-} Baugruppen. *Z. Anorg. Allg. Chem.* **516**, 35–41 (1984).
18. Bronger, W. & Auffermann, G. High pressure synthesis and structure of Na_2PtH_6. *J. Alloy. Compd.* **219**, 45–47 (1995).
19. Karpov, A., Nuss, J., Wedig, U. & Jansen, M. Cs_2Pt: a platinide(-II) exhibiting complete charge separation. *Angew. Chem. Int. Ed.* **42**, 4818–4821 (2003).
20. Arrieta, R. & Brgoch, J. Forming platinide phases under pressure in the Cs–Pt system. *J. Phys. Chem. C* **126**, 2062–2069 (2022).
21. Teherani, T. H., Peer, W. J., Lagowski, J. J. & Bard, A. J. Electrochemical behavior and standard potential of gold(1−) ion in liquid ammonia. *J. Am. Chem. Soc.* **100**, 7768–7770 (1978).
22. Tran, N. E. & Lagowski, J. J. Metal ammonia solutions: solutions containing argentide ions. *Inorg. Chem.* **40**, 1067–1068 (2001).
23. Firman, T. K. & Landis, C. R. Structure and electron counting in ternary transition metal hydrides. *J. Am. Chem. Soc.* **120**, 12650–12656 (1998).
24. Elnagar, M. M., Jacob, T. & Kibler, L. A. Cathodic corrosion of Au in aqueous methanolic alkali metal hydroxide electrolytes: notable role of water. *Electrochem. Sci. Adv.* **2**, 1–11 (2022).
25. Hanselman, S., Calle-Vallejo, F. & Koper, M. T. M. Computational description of surface hydride phases on Pt(111) electrodes. *J. Chem. Phys.* **158**, 014703 (2023).
26. Evazzade, I., Zagalskaya, A. & Alexandrov, V. Revealing elusive intermediates of platinum cathodic corrosion through DFT simulations. *J. Phys. Chem. Lett.* **13**, 3047–3052 (2022).
27. Bratsch, S. & Lagowski, J. Predicted stabilities of monatomic anions in water and liquid ammonia at 298.15 K. *Polyhedron* **5**, 1763–1770 (1986).
28. Hersbach, T. J. P., Yanson, A. I. & Koper, M. T. M. Anisotropic etching of platinum electrodes at the onset of cathodic corrosion. *Nat. Commun.* **7**, 12653 (2016).
29. Hersbach, T. J. P., Mints, V. A., Calle-Vallejo, F., Yanson, A. I. & Koper, M. T. M. Anisotropic etching of rhodium and gold as the onset of nanoparticle formation by cathodic corrosion. *Faraday Discuss.* **193**, 207–222 (2016).
30. Pantelouris, A., Kueper, G., Hormes, J., Feldmann, C. & Jansen, M. Anionic gold in Cs_3AuO and Rb_3AuO Established by X-ray absorption spectroscopy. *J. Am. Chem. Soc.* **117**, 11749–11753 (1995).
31. Vinson, J. Advances in the OCEAN-3 spectroscopy package. *Phys. Chem. Chem. Phys.* **24**, 12787–12803 (2022).
32. Kirklin, S. et al. The Open Quantum Materials Database (OQMD): assessing the accuracy of DFT formation energies. *NPJ Comput. Mater.* **1**, 15010 (2015).
33. Ghebouli, M. A. et al. Theoretical prediction of the fundamental properties for the ternary Li_2PtH_6 and Na_2PtH_6. *J. Solid State Chem.* **196**, 498–503 (2012).
34. Kunimatsu, K., Senzaki, T., Samjeské, G., Tsushima, M. & Osawa, M. Hydrogen adsorption and hydrogen evolution reaction on a polycrystalline Pt electrode studied by surface-enhanced infrared absorption spectroscopy. *Electrochim. Acta* **52**, 5715–5724 (2007).
35. Barber, J., Morin, S. & Conway, B. E. Specificity of the kinetics of H_2 evolution to the structure of single-crystal Pt surfaces, and the relation between opd and upd H. *J. Electroanal. Chem.* **446**, 125–138 (1998).
36. Tan, T. L., Wang, L.-L., Johnson, D. D. & Bai, K. Hydrogen deposition on Pt(111) during electrochemical hydrogen evolution from a first-principles multiadsorption-site study. *J. Phys. Chem. C* **117**, 22696–22704 (2013).
37. Tan, T. L., Wang, L.-L., Zhang, J., Johnson, D. D. & Bai, K. Platinum nanoparticle during electrochemical hydrogen evolution: adsorbate distribution, active reaction species, and size effect. *ACS Catal.* **5**, 2376–2383 (2015).
38. McCrum, I. T., Bondue, C. J. & Koper, M. T. M. Hydrogen-induced step-edge roughening of platinum electrode surfaces. *J. Phys. Chem. Lett.* **10**, 6842–6849 (2019).
39. Ramaker, D. E. & Koningsberger, D. C. The atomic AXAFS and $\Delta\mu$ XANES techniques as applied to heterogeneous catalysis and electrocatalysis. *Phys. Chem. Chem. Phys.* **12**, 5514 (2010).
40. Jerkiewicz, G. Hydrogen sorption at/in electrodes. *Prog. Surf. Sci.* **57**, 137–186 (1998).
41. Stoerzinger, K. A. et al. Probing the surface of platinum during the hydrogen evolution reaction in alkaline electrolyte. *J. Phys. Chem. B* **122**, 864–870 (2018).
42. Chen, X., McCrum, I. T., Schwarz, K. A., Janik, M. J. & Koper, M. T. M. Co-adsorption of cations as the cause of the apparent pH dependence of hydrogen adsorption on a stepped platinum single-crystal electrode. *Angew. Chem. Int. Ed.* **56**, 15025–15029 (2017).
43. Rizo, R. et al. Investigating the presence of adsorbed species on Pt steps at low potentials. *Nat. Commun.* **13**, 2550 (2022).
44. Monteiro, M. C. O. et al. Absence of CO_2 electroreduction on copper, gold and silver electrodes without metal cations in solution. *Nat. Catal.* **4**, 654–662 (2021).
45. Osawa, M., Tsushima, M., Mogami, H., Samjeské, G. & Yamakata, A. Structure of water at the electrified platinum–water interface: a study by surface-enhanced infrared absorption spectroscopy. *J. Phys. Chem. C* **112**, 4248–4256 (2008).
46. Feng, J. et al. Cathodic corrosion of a bulk wire to nonaggregated functional nanocrystals and nanoalloys. *ACS Appl. Mater. Interfaces* **10**, 9532–9540 (2018).
47. Momma, K. & Izumi, F. VESTA 3 for three-dimensional visualization of crystal, volumetric and morphology data. *J. Appl. Crystallogr.* **44**, 1272–1276 (2011).

Methods

Operando XANES measurements

Operando HERFD-XANES experiments of the platinum L_{III} edge were conducted at beamline 6-2 of the Stanford Synchrotron Radiation Lightsource (SSRL). The incoming X-ray beam was monochromatized with a liquid nitrogen-cooled double-crystal Si(311) monochromator. A parabolic Rh-coated mirror delivered this beam to our sample with a height of 420 µm full width at half maximum (FWHM) and a width of 130 µm FWHM. An upstream collimating Rh-coated mirror at 3.5 mrad rejected higher harmonics. We aligned our electrode in grazing incidence, with the electric field vector of the beam parallel to the sample surface. The beam energy was calibrated by assigning a value of 11,563.7 eV to the first inflection point of the Pt L_{III} edge of a Pt reference foil. Following sample irradiation, fluorescent Pt $L_{\alpha 1}$ X-rays (9442 eV) were detected with a Johann-type X-ray spectrometer[48]. These X-rays were diffracted onto the detector by using five spherically bent Ge(660) crystals with a radius of curvature of 1 m. This setup had a combined monochromator and spectrometer resolution of 1.0 eV, as determined by measuring a scattering peak at the Pt $L_{\alpha 1}$ energy and finding its FWHM by fitting a Gaussian peak.

Electrochemical XANES cell

A custom-made flow cell was used for the operando XANES measurements. In this cell, shown in Supplementary Figs. 1 and 2, the working electrode was the lowest point, such that the incoming and fluorescent X-rays could travel towards the sample spectrometer unimpaired. More details of the cell are given in Supplementary Information.

The working electrolyte was 10 mol l^{-1} NaOH (Merck, Suprapur), stored a fluorinated ethylene propylene bottle and pumped into the cell through perfluoroalkoxy alkane tubing. We used Millipore MilliQ water (resistivity >18.2 MΩ cm, total organic carbon <5 µg kg^{-1}) in this work. We used a peristaltic pump (Ismatec IP-N), which was fitted with diameter (ø) = 3.17 mm phthalate-free polyvinyl chloride tubing and operated at a flow rate of 10 ml min^{-1}. The electrolyte flow continuously removed bubbles from the working electrode, thus minimizing the effect of hydrogen bubbles on the acquisition of X-ray absorption spectra.

Within the electrochemical cell channel, a thin Pt (Mateck, 99.9%) counter-electrode was placed alongside the working electrode and a Gaskatel 'HydroFlex' reversible hydrogen electrode (RHE) was placed downstream. The working electrode was a ø = 3 mm gold (Alfa Aesar, 99.9985%) disk containing 22.5 µg of surfactant-free Pt nanoparticles that were drop-casted onto the electrode from an aqueous 0.5 mg ml^{-1} suspension and dried under helium. The nanoparticles adhered to the gold electrode without the use of ionomers (see 'Nanoparticle preparation' section). Before collecting spectra, the nanoparticles were electrochemically pretreated as described in 'Electrochemical data collection' section.

Nanoparticle preparation

Nanoparticles were prepared through cathodic corrosion[4], by applying a 100 Hz square wave potential with −5 V/+2 V versus the RHE potential limits. These potentials were 85% IR-corrected and applied by a Bio-Logic SP-300 potentiostat (connected to a 2 A/30 V booster board) using a HydroFlex RHE electrode (Gaskatel) and a graphite rod (Alfa Aesar, Ultra 'F' purity) counter-electrode. The corrosion electrolyte was 5 mol l^{-1} KOH (Sigma-Aldrich, 99.99% trace metals basis), held within a fluorinated ethylene propylene container. Using this configuration, we immersed a 1 mm length of ø = 0.1 mm Pt wire (Mateck, 99.99%) and corroded it until the wire was consumed. We repeated this step twice and then purified the nanoparticles through ultracentrifugation; the particles were repeatedly centrifuged and the supernatant was replaced with fresh MilliQ water until the supernatant pH was neutral.

The electrochemical synthesis procedure yielded nanoparticle agglomerates between approximately 100 nm and 2,500 nm in length. The primary particles in these agglomerates had a size of 3 ± 1 nm (the error represents one standard deviation), as determined through transmission electron microscopy. Representative micrographs and primary particle size distributions are given in Supplementary Figs. 3 and 4.

The primary particle sizes and agglomeration resemble previous reports of cathodic corrosion as a nanoparticle synthesis method[46]. Particle agglomeration is caused by the absence of a nanoparticle-stabilizing surfactant[46]. This lack of surfactants is crucial for two reasons. First, surfactants could strongly affect the electrochemical behaviour of the studied Pt nanoparticles, thus obscuring any changes caused by cathodic corrosion. Second, surfactant-capped and carbon-supported nanoparticles adhered poorly to the gold working electrode in exploratory experiments. These issues are avoided by not using surfactants.

Experimental setup cleaning

Following previous work[16], we cleaned our electrochemical flow cell by storing it overnight in an aqueous mixture of 1 g l^{-1} $KMnO_4$ (Fluka, ACS reagent) and 0.5 mol l^{-1} H_2SO_4 (Fluka, ACS reagent). We removed this solution before experiments, decomposing any residual $KMnO_4$ with dilute H_2O_2 (Merck, Emprove exp). We then drained this solution and boiled the flow cell parts five times in water.

Electrochemical data collection

After installing the flow cell, its platinum-containing working electrode was pretreated by recording 20 cyclic voltammograms between −0.1 V and 1.7 V_{RHE}, at a scan rate of 250 mV s^{-1}. All potentials were applied and 85% IR-corrected by a Bio-Logic SP-300 potentiostat without a booster board. We then recorded four cycles at 50 mV s^{-1} between 0.06 V_{RHE} and 0.7 V_{RHE}, to validate that the electrochemical response of the platinum nanoparticles matches literature reports. The electrode was then held at a series of constant voltages to enable X-ray absorption data collection; 15 min holds were conducted at 0.4 V_{RHE}, 0.9 V_{RHE} and 1.5 V_{RHE} to reproduce spectral changes occurring when Pt is electrochemically oxidized[16]. We then held the electrode cathodically to probe its behaviour before and during cathodic corrosion: 15 min holds sufficed at 0.0 V and −0.2 V_{RHE}, whereas 30 min holds were required at −0.4 V_{RHE} and below (see 'Data normalization and processing' section). Following cathodic holds, the working electrode was held for 15 min at various voltages at and above 0.4 V_{RHE} to collect spectra to revalidate that our setup functioned appropriately. The electrode was exposed to open-circuit potential for several seconds between potential holds. The series of holds was conducted twice, using a fresh working electrode for each duplicate.

Data normalization and processing

Our custom setup enabled the collection of operando X-ray absorption spectra with high signal-to-noise ratios at potentials above −0.4 V_{RHE}. At these voltages, four spectra were recorded and averaged. More spectra were recorded during substantial hydrogen evolution (−0.4 V_{RHE} and below), to compensate for bubble-induced noise. Spectra with excess noise were eliminated from the analysis; eight scans were averaged per applied potential, and the counting statistics achieved were better than 1% for all spectra. Acceptable and bubble-distorted spectra are shown in Supplementary Fig. 5. Each scan contained 225 data points, which were measured for 0.5 s each. Accounting for the time needed for the monochromator to move between energy positions, it took approximately 3.5 min to record a single scan.

All data were processed according to our previous work[16]. In brief, we aligned our X-ray absorption spectra by aligning the monochromator crystal glitch position of the individual spectra using IgorPro. The spectra were then averaged, flattened and normalized in ATHENA[49]. Indicating this normalization, we plot normalized spectra with *y*-axis units of 'edge fraction'[16]. When smoothing spectra, a boxcar average with a width of five data points was used.

Platinum hydride formation energy calculations

Internal energies and vibrational frequencies were calculated using version 5.4.4 of the Vienna Ab initio Simulation Package (VASP) for various *H configurations on Pt(111)[50]. Initial configurations were obtained by systematically sampling different initial positions of surface Pt and (sub)surface *H for various *H coverages in a four-layer 3 × 3 Pt(111) slab, with the lowermost two layers fixed to bulk interatomic distances, as described by Hanselman et al.[25]. The internal energies are derived from ground-state DFT geometry optimizations, and vibrational frequencies were calculated for the energetically most stable configurations using single-atom displacements of H atoms and surface Pt atoms. The DFT plane-wave basis cutoff energy was set to 33.1 Ry (450 eV), and all calculations were performed using plane augmented waves, the Perdew–Berke–Ernzerhof (PBE) functional and projector-augmented-wave (PAW) pseudopotentials as supplied in VASP 5.4.4. The Brillouin zone was sampled using a 2 × 2 × 1 Monkhorst–Pack grid, and Kohn–Sham orbital densities were smeared by 0.2 eV using the first-order Methfessel–Paxton method. We subjected the most stable configurations to symmetry analysis; the corresponding translational, rotational and mirror symmetries were added to the internal energies and vibrational free energies derived from the vibrational frequencies to obtain the full free formation energy for the most stable configuration for each *H coverage. A detailed description of this method is presented in the work of Hanselman et al.[25].

First-principles XANES spectrum simulation

Calculations of core-level spectra were performed within OCEAN version 3.1.1 (ref. 31). This code calculates X-ray absorption spectra within a plane-wave DFT formalism that explicitly accounts for excitonic effects within the Bethe–Salpeter equation approach. As input structures for these XANES calculations, we used experimental structures of metallic Pt (ref. 51), α-PtO_2 (ref. 52), Na_2PtH_4 (ref. 17) and Na_2PtH_6 (ref. 33). Structures of $NaPt_2$, NaPt and Na_2Pt were acquired from the Open Materials Quantum Database[32]. We also used platinum surfaces with one to four MLs of hydrogen from our own work[25]. All bulk systems were fully relaxed (unit cell and atomic positions) using the QUANTUM ESPRESSO package version 7.0 with DFT at the generalized gradient approximation (GGA-PBE) level with a kinetic plane-wave energy cutoff of 104 Ry; we used norm-conserving pseudopotentials from PseudoDojo (v0.4 stringent accuracy, scalar-relativistic PBE)[53], generated with the ONCVPSP code[54], modified for OCEAN (https://github.com/jtv3/oncvpsp). The reciprocal space of the systems was regularly sampled to divide lattice vectors into segments shorter than 0.09 $a.u.^{-1}$. We converged the wave functions to a self-consistent field threshold of 10^{-13} and determined electronic occupancies by the Fermi–Dirac method using 0.001 Ry smearing. All input structures for results in the main text are visualized in Supplementary Figs. 6, 7 and 11. For the final Bethe–Salpeter equation states, each grid was chosen to divide the reciprocal lattice vectors into segments below 0.12 $a.u.^{-1}$. For the supercell adsorbate-covered surface slabs, the *k*-point grid used for ground- and final state calculations was 4 × 4 × 1. The number of conduction bands was set such that the highest unoccupied state was approximately 80 eV above the lowest unoccupied state. We ensured that screening parameters were well converged so that accurate values for the relative exciton positions were obtained: a radius of 12 a.u. was chosen for the neutralizing shell that separates the random-phase approximation and model calculations of the screening response. This was done to reduce errors in the core-level shift from inaccuracies in the model dielectric, which scale as the inverse of this radius[55]. For all bulk systems, the screening *k*-point mesh was set to exceed the sampling density of 0.35 $a.u.^{-1}$. For the surface structures, a *k*-grid of 2 × 2 × 2 was used for the screening calculations. For all systems, the number of unoccupied bands includes the first 200 eV above the conduction band minimum. For calculating the spectra, the real-space regular grid was set to divide lattice vectors by less than 0.84 a.u. for the bulk structures, and a real-space grid of 12 × 12 × 48 for the surfaces. The calculated Pt L_{III} edge spectra were numerically broadened via convolution using Lorentzian and Gaussian functions with a 0.6 eV half width at half maximum and a 1.6 eV FWHM, to match the HERFD-XANES broadening. When comparing periodic bulk systems, the core-level shift was obtained through calculations for Pt metal and applied to the other bulk compounds. When comparing surfaces, the core-level shift was found for adsorbate-free surfaces and applied to adsorbate-covered ones. Then, a single constant energy shift was applied to align the simulated spectra with experimental data. Specifically, the calculated Pt spectrum was shifted to have its whiteline position match that of the experimental spectrum at 0.4 V_{RHE}: 11,565.35 eV. The same absolute shift was applied to the other calculated spectra. All bulk structures were aligned using the OCEAN spectrum for bulk Pt, whereas the surfaces were aligned using the OCEAN spectrum of the third atomic layer of a bare Pt slab; for slabs, the third-layer spectrum of bare Pt most closely resembles our experimental Pt spectrum. Finally, to validate our computational approach, we compared our Open Quantum Materials Database-based OCEAN spectra with those generated using geometries from the Materials Project database and experimental crystal structures (Supplementary Fig. 12).

Data availability

All data used for this study are available within the Article and its Supplementary Information. Source data are provided with this paper. The data files are also available from the corresponding authors upon request.

References

48. Sokaras, D. et al. A seven-crystal Johann-type hard X-ray spectrometer at the Stanford Synchrotron Radiation Lightsource. *Rev. Sci. Instrum.* **84**, 053102 (2013).
49. Ravel, B. & Newville, M. ATHENA, ARTEMIS, HEPHAESTUS: data analysis for X-ray absorption spectroscopy using IFEFFIT. *J. Synchrotron Radiat.* **12**, 537–541 (2005).
50. Kresse, G. & Furthmüller, J. Efficient iterative schemes for ab initio total-energy calculations using a plane-wave basis set. *Phys. Rev. B* **54**, 11169–11186 (1996).
51. Swanson, H. E. & Tatge, E. *Standard X-Ray Diffraction Powder Patterns* (US Government Printing Office, 1953).
52. McBride, J. R., Graham, G. W., Peters, C. R. & Weber, W. H. Growth and characterization of reactively sputtered thin-film platinum oxides. *J. Appl. Phys.* **69**, 1596–1604 (1991).
53. van Setten, M. J. et al. The PSEUDODOJO: training and grading a 85 element optimized norm-conserving pseudopotential table. *Comput. Phys. Commun.* **226**, 39–54 (2018).
54. Hamann, D. R. Optimized norm-conserving Vanderbilt pseudopotentials. *Phys. Rev. B* **88**, 1–10 (2013).
55. Vinson, J. & Shirley, E. L. Fast, efficient, and accurate dielectric screening using a local real-space approach. *Phys. Rev. B* **103**, 1–24 (2021).

Acknowledgements

We acknowledge M.-Y. Wu from MYAnalysis for assisting with transmission electron microscopy measurements. Certain equipment, instruments, software or materials, commercial or non-commercial, are identified in this Article to specify the experimental procedure adequately. Such identification is not intended to imply recommendation or endorsement of any product or service by NIST, nor is it intended to imply that the materials or equipment identified are necessarily the best available for the purpose. Use of the Stanford Synchrotron Radiation Lightsource, SLAC National Accelerator Laboratory, is supported by the US Department of Energy, Office of Science, Office of Basic Energy Sciences under contract no. DE-AC02-76SF00515. This work was supported in part by the Netherlands Organization for Scientific Research (NWO) in the framework of the Solar Fuels Graduate Program. The use of supercomputing facilities at SURFsara was sponsored by NWO Physical Sciences, with financial support by NWO. OCEAN simulations were performed using resources of the National Energy Research Scientific Computing Center (NERSC), a US Department of Energy Office of Science User Facility operated under contract no. DE-AC02-05CH11231.

Author contributions

T.J.P.H., D.S. and M.T.M.K. designed the experimental study. T.J.P.H. conducted and coordinated most of the experimental work, data analysis and data reduction. A.T.G.-E., O.A.P.M. and J.V. performed the OCEAN simulations activities. S.H. and I.T.M. generated the platinum surfaces for first-principles calculations. A.T.G.-E., D.A., J.T.F., T.F.J., A.C.G., P.K., T.K. and D.S. participated in the experimental work. T.H. designed the operando grazing incidence cell. T.J.P.H. led the drafting of the manuscript, with contributions from A.T.G.-E., S.H., J.V., D.S. and M.T.M.K. for editing. D.S. and M.T.M.K. supervised the work and obtained funding and resources. All authors discussed the results and the manuscript.

Competing interests

The authors declare no competing interests.

Additional information

Supplementary information The online version contains supplementary material available at https://doi.org/10.1038/s41563-024-02080-y.

Correspondence and requests for materials should be addressed to Dimosthenis Sokaras or Marc T. M. Koper.

Peer review information *Nature Materials* thanks Marcel Risch and the other, anonymous, reviewer(s) for their contribution to the peer review of this work.